RSC Advances

PAPER

View Article Online
View Journal | View Issue

Cite this: *RSC Adv.*, 2023, **13**, 34145

The effects of electrodeposition temperature on morphology and corrosion resistance of calcium phosphorus coatings on magnesium alloy: comparative experimental and molecular dynamics simulation studies

Jing Yuan, *[a] Bin Dai,[a] Xiaofeng Cui[a] and Pei Li*[b]

In this study, CaP coatings were prepared on the surface of an AZ31B magnesium alloy using electroplating in order to slow down the degradation rate of magnesium alloy in the simulated physiological environment. The effect of plating temperature on the properties of CaP coatings was investigated by combining experimental techniques with molecular dynamics (MD) simulation. The surface morphology of CaP coatings changed from dendritic lamellar to granular structure with the increase of plating temperature, but the main structure of CaP coatings prepared at all temperatures was $CaHPO_4 \cdot 2H_2O$. The CaP coatings prepared at 60 °C have higher corrosion resistance compared to coatings prepared at other temperatures. The MD simulation revealed the DCPD/Mg interfacial binding mechanism, and DCPD/Mg could form a stable interfacial layer at different temperatures because the binding energy was negative. HPO_4^{2-} and H_2O groups in the DCPD structure acted as riveting groups in the interfacial layer and formed Mg–HPO_4^{2-} and Mg–H_2O dipole pairs with Mg respectively through electrostatic interaction and van der Waals forces. The interfacial bonding energy between DCPD/Mg reached its lowest at 60 °C and the relative contents of HPO_4^{2-} and H_2O in the interface layer were the highest at this temperature, which may explain the high corrosion resistance and high bonding force of CaP coatings prepared at this temperature.

Received 21st June 2023
Accepted 16th November 2023

DOI: 10.1039/d3ra04162j

rsc.li/rsc-advances

1. Introduction

Magnesium and its alloys can be degraded in a physiological environment, and their mechanical properties such as density and elastic modulus close to those of the cortical bone have important application prospects as orthopedic implants.[1–3] Despite the above advantages, there are two significant drawbacks which prevent their large-scale application in clinical applications. One is that the rate of degradation of magnesium and its alloys in the physiological environment exceeds bone healing rate, and the other is their low biological activity.[4,5] Many strategies have been adopted to improve the biological activity and corrosion resistance of Mg-based alloys, such as development of Mg–Ca alloys, and exploration of new casting techniques and coatings.[6–8]

Bioactive coatings, especially calcium–phosphorus (CaP) coatings, which are similar to the main mineral components of human bones, not only acts as a barrier layer, but also promote the growth of natural bone cells.[9,10] The CaP coatings generally include DCPD ($CaHPO_4 \cdot 2H_2O$), TCP ($Ca_3(PO_4)_2$), OCP ($Ca_8H_2(PO_4)_6 \cdot 5H_2O$) and HA ($Ca_{10}(PO_4)_6(OH)_2$). Among them, DCPD and HA coatings reveal greater biocompatibility properties as has been reported by previous studies.[11] Several techniques have been reported to deposit CaP coatings on magnesium alloys, including sol–gel process, chemical conversion methods, micro arc oxidation process, hydrothermal and electrodeposition.[12–16] Electrodeposition is widely used for prepare Mg-based coatings because the process involves simple, controllable and able to obtain uniform coating on the complex shape matrix. Moreover, the coating thickness, morphology, structure and component can be optimized by varying the plating parameters, temperature, pH and electrolyte composition. Horynová *et al.* fabricated CaP coating on pure magnesium substrate by potentiostatic electrodeposition of −3 V and −5 V, and reported that the chemical composition obtained at both voltages were DCPD, but the morphologies was different.[17] The coating prepared at the lower potential was more denser and uniform, and the coating formed at the higher potential became coarser due to a faster deposition process. The effect of the current density on the formation and characteristics of CaP coating was also investigated and found that the CaP coating

[a]*Qinghai Provincial Key Laboratory of Nanomaterials and Technology, Qinghai Minzu University, Xining, Qinghai 810007, P. R. China. E-mail: yuanjing860519@163.com*
[b]*Department of Orthopedic, Qinghai Provincial People's Hospital, Xining, Qinghai, 810000, P. R. China*

exhibits a dense, uniform structure and higher corrosion resistance at low current density of 3 mA cm^{-2} as opposed to porous, uneven and lower corrosion resistance at high current density of 6 and 13 mA cm^{-2}.[18] Above all, the CaP coatings prepared at low potential and low current density have denser structure, more uniform thickness and higher corrosion resistance. Temperature is also one of the important factors affecting corrosion resistance and the adhesion of the CaP coating. Pastorek *et al.* found the CaP coating created by electroplating process at temperatures from 10 to 50 °C was formed by irregular branched units that overlap each other, and the highest corrosion resistance was obtained at about 30 °C.[19] Lu *et al.* fabricated CaP electroplating at different temperatures from 20 to 60 °C, and found the coating deposited at 60 °C exhibited the best corrosion resistance.[20] These studies were aimed to optimizing the preparation temperature and found that Ca–P coatings prepared at temperatures higher than room temperature possessed a denser structure and a homogeneous surface. However, they have not discussed the micro-interface binding mechanism of Mg/DCPD at different temperatures. Moreover, there is little literature discussing the effect of microscopic variables at the Mg/DCPD interface such as binding mode, action site and binding energy on the bonding and corrosion resistance of CaP coatings.

Molecular dynamics simulation (MD) has become an effective strategy to study the structure, properties and interface bonding mode of metal/inorganic (organic) coating composite systems in the past decade.[21–23] Wang *et al.* used MD to study the effect of the second phase on protein adsorption on Mg alloys surface and the results revealed the adsorption mechanism of proteins varied with the charge distribution of the second phase, the interaction between surface and proteins, and the distribution of water molecules.[24] Shang *et al.* investigated the adsorption mechanism of three organic molecules on magnesium-based electroless Ni–P coating, and found the adsorption energy and the binding energy between the coating and organic molecules might affected by oxygen-containing functional groups.[25] Wang *et al.* studied the adsorption behavior of Ca and P atoms on different crystal planes of hydroxyapatite by using MD simulation.[26]

In this work, CaP coatings with different plating temperatures were prepared on the AZ31B magnesium alloy in potentiostatic mode at the lower potential of −2 V. The effects of temperature on the morphology, structure, corrosion resistance and microscopic interface bonding mechanism of the CaP coatings were studied carefully by experiments and computer simulation. This purpose of this work is to reveal the mechanism of the effect of plating temperature on the bonding and corrosion resistance of CaP coatings, and to optimize the preparation process for preparing CaP coatings on the surface of magnesium alloy.

2. Experimental

2.1 Materials

The AZ31B magnesium alloy, its main chemical composition containing Al (2.5–3.5 wt%), Zn (0.6–1.4 wt%), Mn (0.2–1.0 wt%) and balanced Mg was cut into rectangular blocks with the dimensions of 10 × 10 × 4 mm^3, then continuously polished with SiC grit paper from 200 to 1500, cleaned with alcohol ultrasonically for 10 min and dried for plating.

2.2 Electroplating calcium phosphorus coatings

The electroplating electrolyte was consists of 0.1 mol L^{-1} $Ca(NO_3)_2 \cdot 4H_2O$ and 0.06 mol L^{-1} $NH_4H_2PO_4$, and the pH of the solution was adjusted to 5.0 by H_2O_2. A three-electrode system with the magnesium alloy as working electrode, a platinum electrode as counter electrode and a saturated calomel electrode (SCE) as reference electrode was used during electroplating. A constant voltage mode was used during electroplating, the plating voltage was set at −2 V, the plating temperature was varied from 50 °C to 80 °C, and the electroplating time is kept constant for 60 min. The electrolyte was magnetically stirred during electroplating, and the coatings were removed from the solution and dried at the ambient temperature after electroplating.

2.3 Characterization

Surface morphology, thickness and compositions of the prepared coatings were observed by Nova NanoSEM scanning electron microscopy (SEM) equipped with energy dispersive spectroscopy (EDS) at an accelerating voltage of 20 kV. The structure of coatings was measured by X-ray diffractometer (XRD, Empyrean, $\lambda = 1.542512$ nm) at a scan speed of 5° min^{-1} in the 2θ range of 10–90°. The functional groups on the coatings were identified by Thermo Scientific Nicolet iS20 Fourier-transform infrared (FT-IR) spectroscopic analysis. The state of elements present in the outermost parts of the coating were investigated by X-ray photoelectron spectroscopy (XPS, Thermo Scientific K-Alpha).

The polarization curve and electrochemical impedance spectroscopy (EIS) were measured in Hank's solution at 37 °C using Autolab 302 electrochemical workstation, and Hank's solution were prepared as in ref. 27. A three-electrode system with the coated CaP samples by an exposed area of 1 cm^2 as working electrode, a platinum electrode as counter electrode and a saturated calomel electrode (SCE) as reference electrode was employed in the test. The potentiodynamic polarization experiments were performed at a scan rate of 0.1667 mV s^{-1}. The corrosion potential E_{corr} and corrosion current density i_{corr} were estimated by using standard Tafel extrapolation technique from the experimental potentiodynamic polarization plots. And EIS measurements were recorded from 100 kHz to 0.1 Hz with a 10 mV amplitude AC signal at the open circuit potential. The electrochemical parameters for the EIS data were calculated by applying Nova 2.1 software under the given equivalent circuits.

2.4 Molecular dynamics simulation

Based on the XRD data, the main phase of the experimentally prepared Ca–P coating was $CaHPO_4 \cdot 2H_2O$ (DCPD). According to Abbona *et al.* the most common crystal forms in $CaHPO_4 \cdot 2H_2O$ were (010), (−120), (11−1) and (111), with the (−120) facet having the lowest energy.[28] Therefore, the $CaHPO_4 \cdot 2H_2O$ (−120)

crystal plane was used for binding with Mg substrate. Although the substrate used in the experiments was an AZ31 Mg alloy, it had a magnesium content of up to 90%. To further simplify the simulation system, pure Mg substrate was used instead of Mg alloy. And the commonly used Mg (0001) crystal surface was chosen as another bonding surface.[29]

In this paper, MD simulation was used to study the effect of temperature on the bonding of Ca–P coatings to Mg substrates. The simulation was carried out through the Forcite tools using the Consistent Valence Force Field (CVFF).[30] The modeling lattice parameters of $CaHPO_4 \cdot 2H_2O$ (monoclinic crystal and crystal cell parameters were 5.837 × 15.192 × 6.265 ⟨90.0° × 116.47° × 90.0°⟩) were referenced to the studies of N. A. Curry and C. A. Beevers.[31,32] The specific modeling steps were as follow: first, the cells of $CaHPO_4 \cdot 2H_2O$ and Mg were established (Fig. 1(a) and (b)); second, the Cleave Surface tool was used to cut the crystal surface to obtain $CaHPO_4 \cdot 2H_2O$ (−120) and Mg (0001) (Fig. 1(c) and (d)); third, for lattice parameter matching, lattice parameter tunning and supercell processing were performed on the DCPD and Mg interface. Finally, the Build Layers tools was conducted to construct DCPD/Mg system. To avoid the possible molecular overlap, the initial model was optimized using Smart algorithm with 50 000 steps to obtain the optimized structure. The lower two layers of Mg atoms were constrained as the bulk phase and the upper two layer of Mg atoms were regard as the interface phase. And then the NVT dynamic equilibration were running for 10 ns with time step 1 fs under 298 K, 323 K, 333 K, 343 K and 353 K. The Nóse–Hoover method was employed to maintain the temperature and pressure fluctuating around desired constant values and long-range electrostatics was handled by the Ewald method.

3. Results

3.1 Morphologies of calcium phosphorus coatings

Fig. 2 shows the electrodeposited CaP coatings prepared at different temperatures with plating voltage of −2 V. It can be found the plating temperature has a great influence on the morphology of CaP coatings.[33] And the morphology of the coatings prepared at different temperatures varies greatly. In general, the coating consists of two structural layers, the underlying structure is very thin and the polished magnesium substrate can be seen, and showing a dry riverbed-like morphology. The top structure is composed of dendritic lamellar grains with sizes range from tens to hundreds of microns. As the temperature increases from 50 °C to 60 °C, the coverage of dendritic lamellar grains on the surface increases while the size decreases. Apparently, the calcium–phosphorus plating prepared at 70 °C showed inhomogeneity of the deposit and higher roughness. When the temperature is raised to 80 °C, the dendritic lamellar grains disappear and are replaced by granular grains, and the bonding force of the coating drops sharply, and some of the coating peels off when touched by hand. The increase of the plating solution temperature makes the movement of discharge ions in the charge transfer process faster, which accelerates the adsorption of atoms in the crystal formation process and reduces the concentration

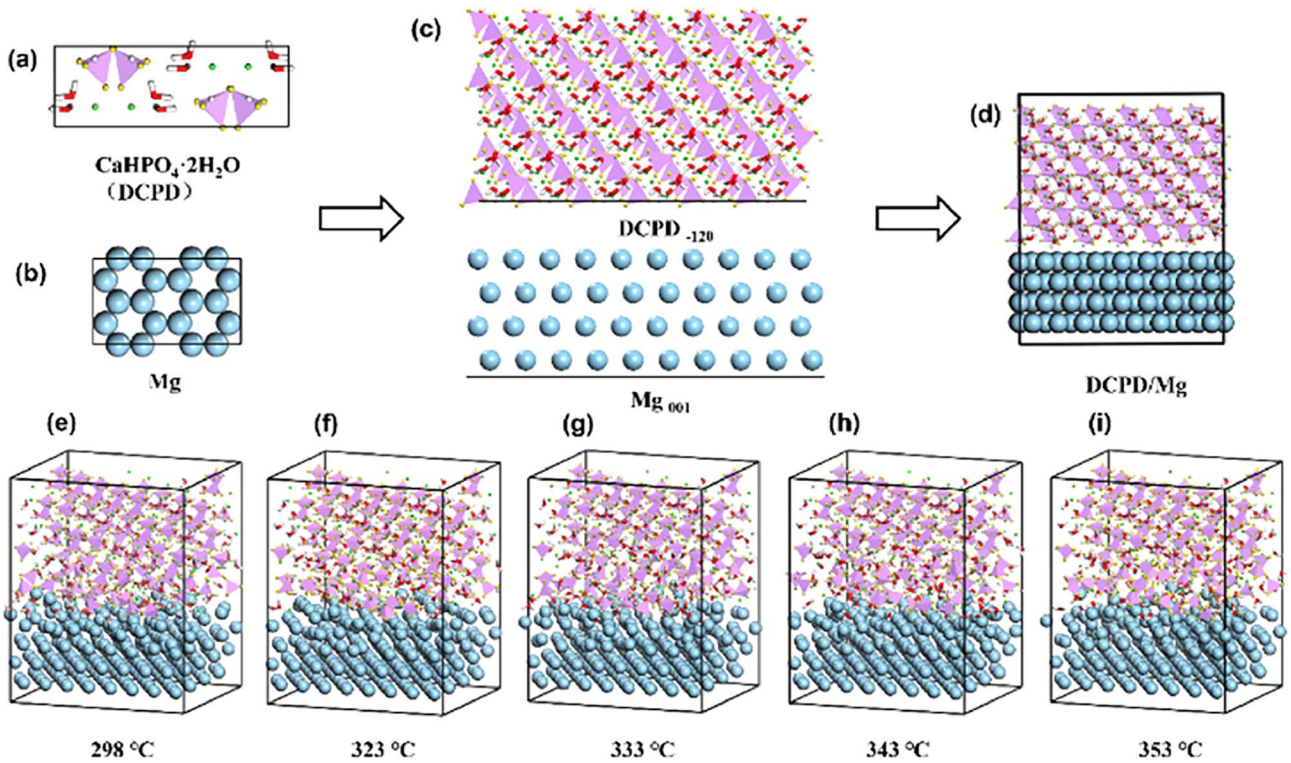

Fig. 1 Schematic diagram of the cell structure and crystal surface structure of $CaHPO_4 \cdot 2H_2O$ and Mg (a and b), and its DCPD/Mg composite system (c and d) at different temperatures (e–i) (blue ball is Mg, red ball is O, green ball is Ca and pink is P in the figure).

polarization. Therefore, when the temperature is low, the Ca^{2+} ion transfer resistance in the plating solution is high, the crystallinity is low, and the grain size is large. As the plating temperature increases, the concentration polarization decreases, and the Ca^{2+} ion transfer resistance is low, which is conducive to the formation of fine, dense grains. However, when the plating temperature is too high, the corrosion resistance of the substrate decreases, and excessive hydroxyl aggregation may cause $Mg(OH)_2$ to be deposited on the surface of the substrate thus affecting the deposition of the CaP coating.[34] The EDS results also reflect a significant difference in the composition content of the coatings prepared at different temperatures. The highest content of Ca and P elements and the lowest content of Mg elements in the coatings prepared at 60 °C indicate that the CaP coatings prepared under this condition have the highest coverage of the magnesium substrate. However, when the temperature is increased to 70–80 °C, the increase in the content of elemental Mg may be due to the surface generation of $Mg(OH)_2$.

Fig. 3 is the mapping of the CaP coatings prepared at different temperatures. The main elements detected in the coatings are Ca, P, Mg, O and Al, but the content of these elements varies with temperature. The main components of

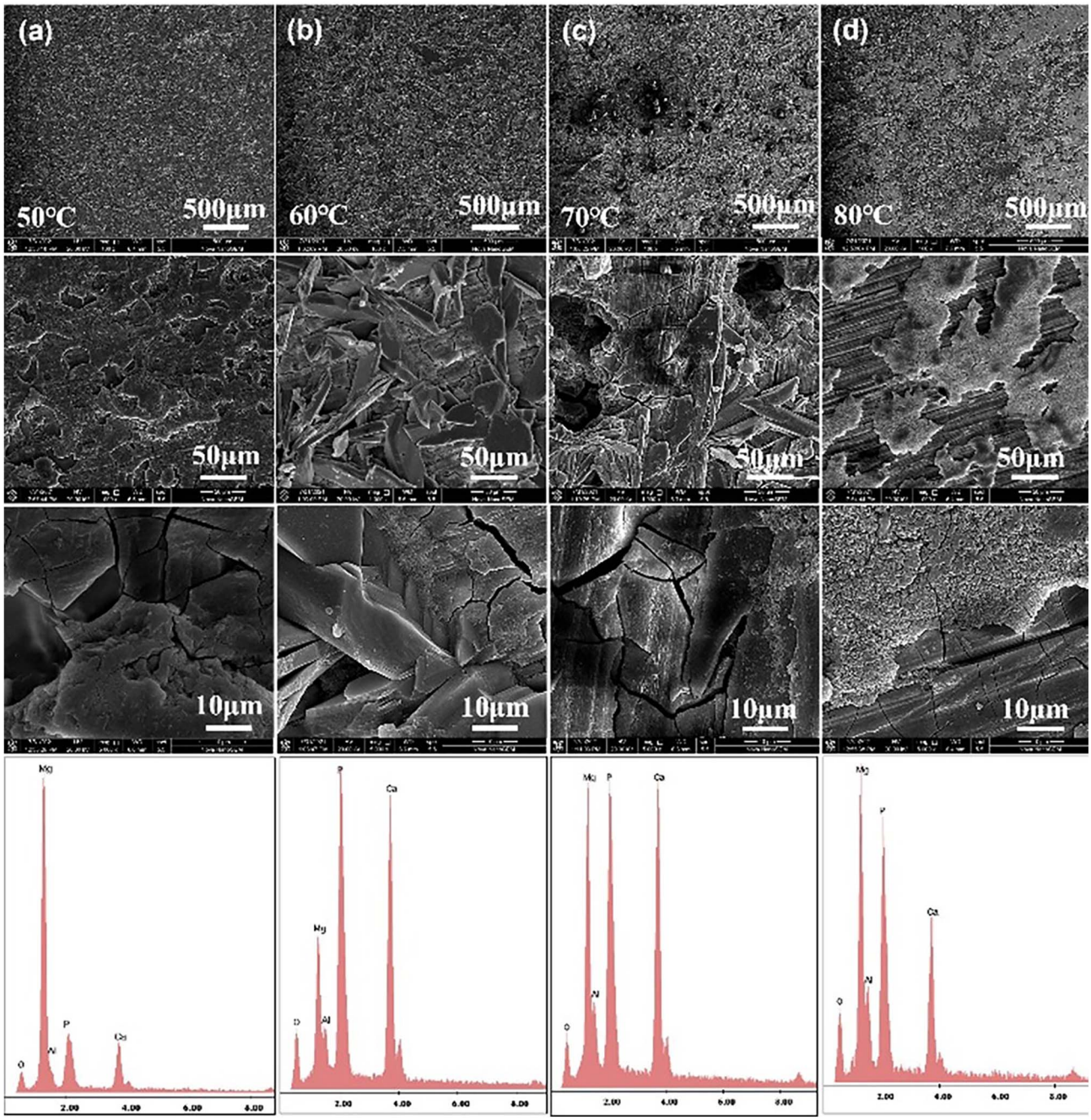

Fig. 2 The SEM images and the EDS results of electroplating CaP coatings with different temperature, (a) 50 °C, (b) 60 °C, (c) 70 °C and (d) 80 °C.

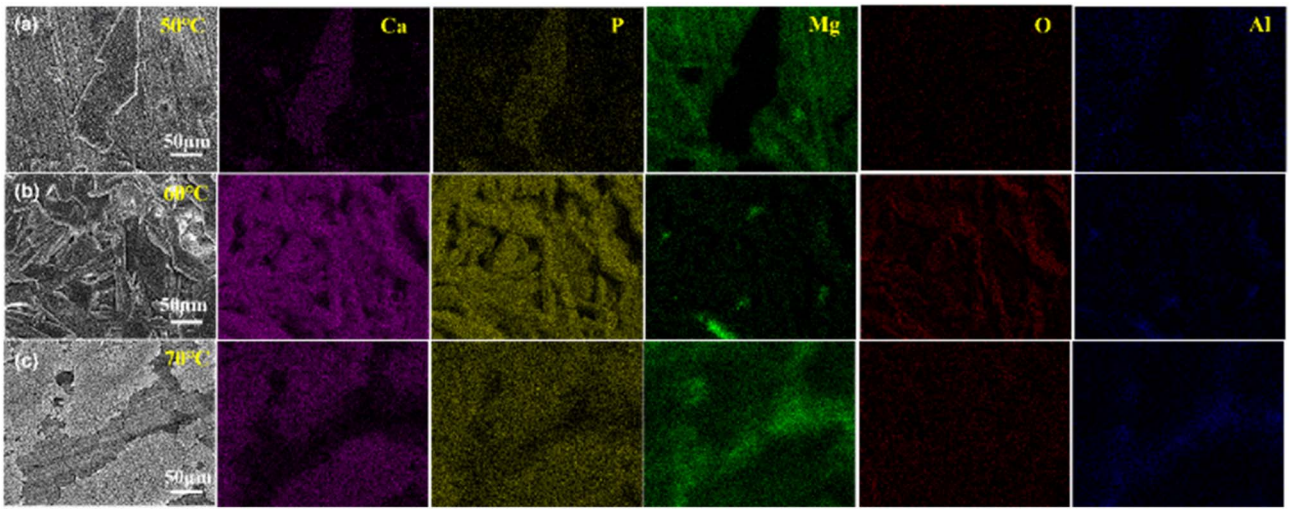

Fig. 3 The mapping images of electroplating CaP coatings with different temperature, (a) 50 °C, (b) 60 °C and (c) 70 °C.

dendritic lamellar grains (50–70 °C) or granular grains (80 °C) on the surface of the coating are Ca and P, but the thin bottom layer contains little Ca. The mapping results indicates that the surface of the magnesium substrate is uniformly covered with dendritic Ca–P structure when the plating temperature is applied at 60 °C.

Fig. 4 is the cross-sectional view of the CaP coatings prepared at different temperatures. The thickness of the coating increases but the uniformity decreases with increasing temperature, and micropores and defects are randomly distributed in the coating. With rising the electroplating temperature, the viscosity and surface tension of water decreased, and the mobility of molecules and ions in solution increased, thereby allowing crystals to grow faster. Therefore, the average thickness of the CaP coating deposited at 60 °C is thicker than that of the sample prepared at 50 °C.

3.2 Structure and chemical composition of calcium phosphorous coatings

In order to characterize the phase structure, the CaP coatings prepared at different temperatures are characterized by XRD in Fig. 5. The diffraction peaks of the AZ31B substrate mainly originate from α-Mg phase (PDF 35-0821). The XRD patterns of CaP coatings show strong diffraction peaks at 11.7°, 18.0°, 20.9°, 23.4°

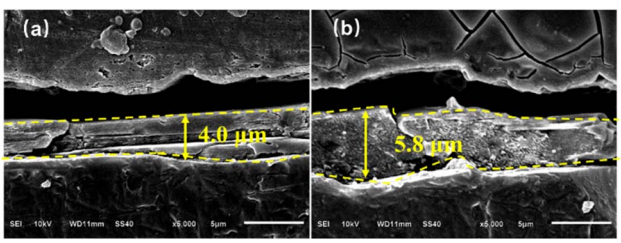

Fig. 4 The cross-section images of electroplating CaP coatings with different temperature, (a) 50 °C, (b) 60 °C.

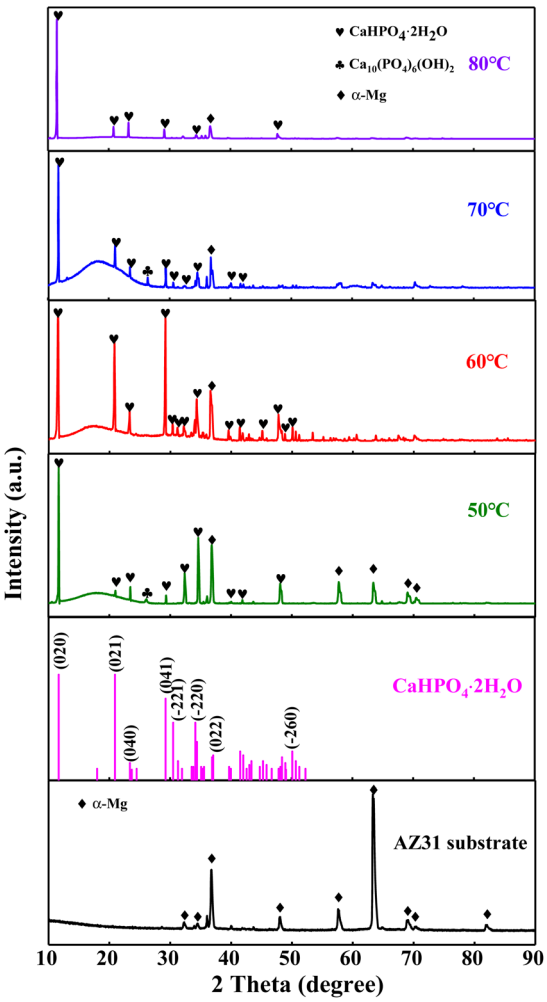

Fig. 5 XRD patterns of CaP coatings at different temperature. The results indicated that the dominant phase of the CaP coatings is DCPD, in addition to a small amount of HA.

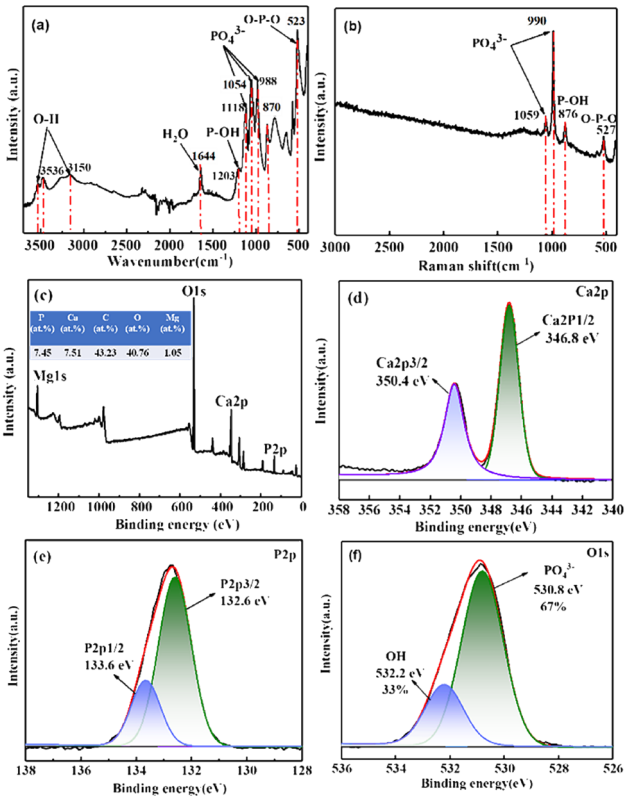

Fig. 6 (a) FTIR spectra, (b) Raman spectra, (c) XPS survey spectra, and (d–f) the high-resolution XPS spectra of Ca, P and O of CaP coating prepared at 60 °C.

and 29.3° which are attributed to (020), (−111), (021), (040) and (041) planes of DCPD phase ($CaHPO_4 \cdot 2H_2O$, PDF 09-0077), and the tiny diffraction peak at 25.9° is ascribed to (002) plane of HA phase ($Ca_{10}(PO_4)_6(OH)_2$, PDF 09-0432).

The FTIR spectra of the CaP coating prepared at 60 °C is shown in Fig. 6(a). Reflection bands at 3536–3150 cm^{-1} regions are attributed to two O–H stretching doublets, indicating the presence of water crystals in the lattice structure.[35] H_2O bending bands are located at 1644 cm^{-1}, while the libration bands are seen at 784 cm^{-1} and 648 cm^{-1}.[35] In addition, the reflection peaks at 1118 cm^{-1}, 1054 cm^{-1} and 988 cm^{-1} are confirmed the phosphate triplet.[27] And the peaks at 1203 cm^{-1} and 870 cm^{-1} are ascribed to P–OH in plane bending and stretching modes.[27] Reflection band at about 523 cm^{-1} are due to P–O–P bending mode.[36]

Fig. 6(b) is the Raman spectra of the CaP coating prepared at 60 °C. The scattering peaks at 1059 cm^{-1} and 990 cm^{-1} are assigned to PO_4^{3-} stretching mode, and the peak at 876 cm^{-1} are attributed to P–OH stretching mode.[37] Besides, the peak at 527 cm^{-1} is confirmed the bending mode of O–P–O group.[38] Both the FTIR and the Raman spectra confirm that the CaP compound uniformly covering on the surface of the AZ31 substrate is DCPD ($CaHPO_4 \cdot 2H_2O$), which is consistent with the XRD results.

Fig. 6(c) is the XPS survey spectra of CaP coating prepared at 60 °C and the high-resolution spectra of Ca 2p, P 2p and O 1s are shown in Fig. 6(d)–(f), respectively. The Mg, O, Ca and P

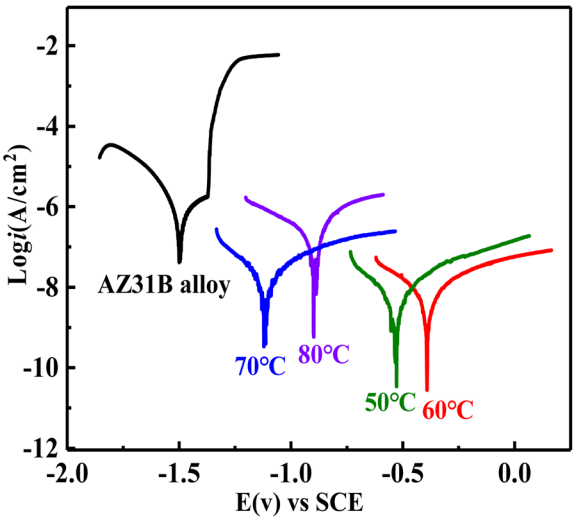

Fig. 7 The potentiodynamic polarization evaluation of the DCPD coatings on AZ31B magnesium alloy substrate.

elements are detected on the surface of the DCPD coating as shown in Fig. 6(c), and Ca/P ratio of the CaP coating determined by XPS is approximately 1.01, which is close to the theoretical Ca/P atomic percentage of DCPD.[39] The Ca 2p high-resolution spectra in Fig. 6(d) can be split into Ca $2p_{3/2}$ and Ca $2p_{1/2}$ resolution peaks are located at 346.8 eV and 350.4 eV, which are the typical two peaks of Ca^{2+}.[40] The P 2p high-resolution spectra in Fig. 6(e) consists of P $2p_{3/2}$ and P $2p_{1/2}$ resolution peaks are located at 132.6 eV and 133.6 eV respectively, which are corresponding to PO_4^{3-}.[40] And the O 1s high-resolution spectra in Fig. 6(f) can be divided into two peaks located at 530.8 eV and 532.2 eV, which are mainly corresponding to PO_4^{3-} and OH^-, and the corresponding percentage of O–P and O–H group is 67% and 33% respectively, which close to the composition of functional groups in DCPD. According to the XPS results, the main composition of the coating is DCPD.

3.3 Corrosion resistance

To evaluate the corrosion resistance of the CaP coatings on AZ31B magnesium alloy, the potentiodynamic polarization curves and EIS measurements were performed in SBF solution at 37 °C in this work. Fig. 7 is the potentiodynamic polarization curves of the AZ31B substrate and the CaP coatings prepared at different plating temperatures, and E_{corr} and i_{corr} values are derived from the polarization curves by means of Tafel

Table 1 E_{corr} and i_{corr} of the CaP coatings obtained by polarization curve fitting

Samples	E_{corr} (mV)	i_{corr} (μA cm^{-2})
AZ31B	−1498.2	7.96×10^{-1}
50	−527.7	8.55×10^{-3}
60	−390.2	4.89×10^{-3}
70	−1118.6	1.70×10^{-2}
80	−896.5	2.09×10^{-1}

extrapolation method are shown in Table 1. Compared with the bare AZ31B magnesium alloy substrate, the corrosion potential of the magnesium alloy substrate prepared with DCPD coating is positively shifted, indicating the corrosion tendency of the AZ31B substrate is reduced after the preparation of the coating. In addition, the corrosion current density of the CaP coatings was reduced compared to the substrate. Among these four coatings, the CaP coating prepared at 60 °C has the lowest corrosion current density, which is two orders of magnitude lower than that of the bare AZ31B substrate, and has the best

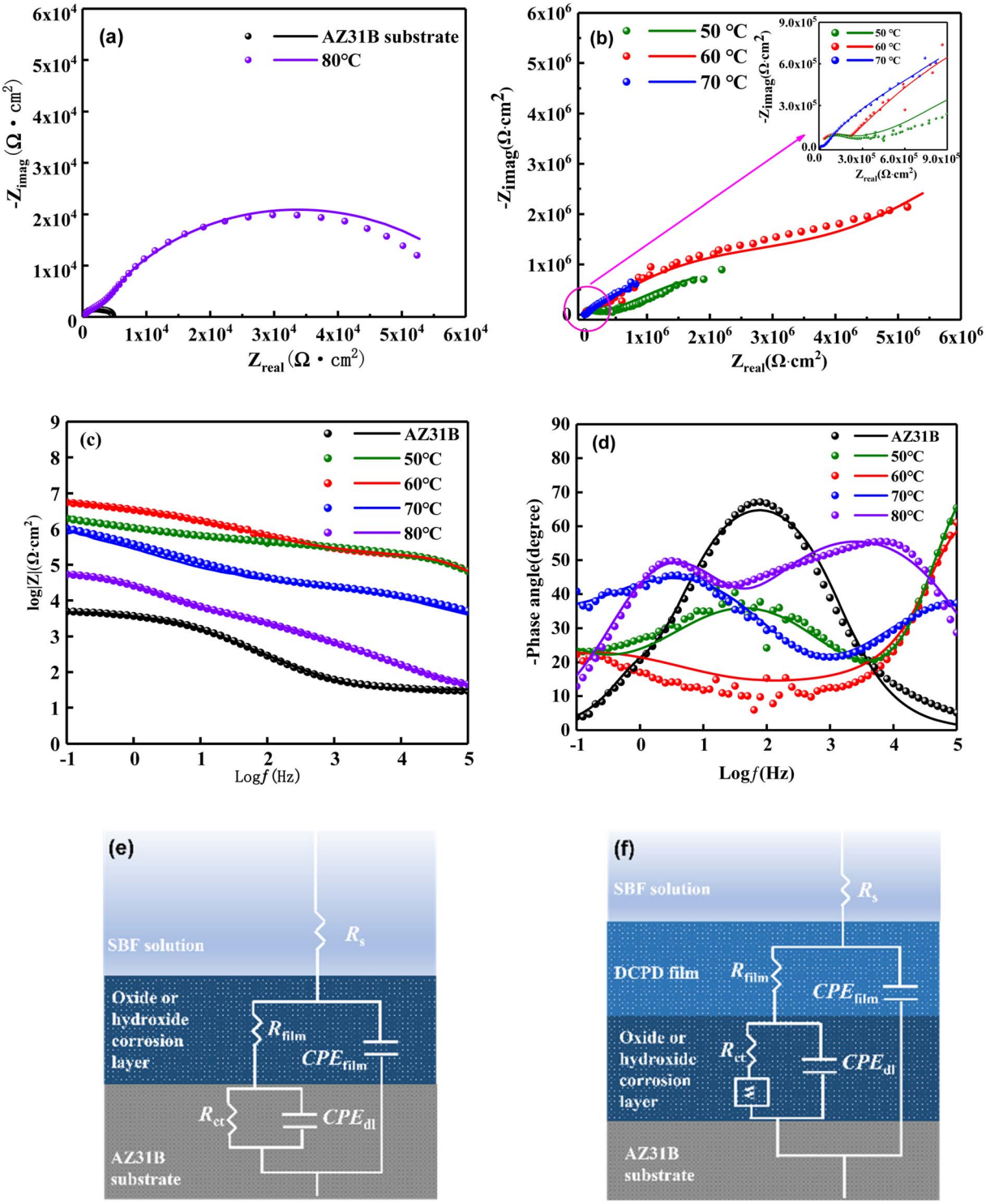

Fig. 8 EIS fitting plots of the bare AZ31B alloy and the DCPD coatings. (a and b) Nyquist spectra, (c) log|*Z*| *vs.* frequency and (d) Bode plots. The equivalent circuit of (e) bare AZ31B alloy and (f) the CaP coating.

Table 2 EIS fitting parameters of composite coatings in SBF solution at 37 °C

Samples	CPE_{film} (S s^n cm^{-2})	n_{film}	R_{film} (Ω cm^2)	CPE_{dl} (S s^n cm^{-2})	n_{ct}	R_{ct} (Ω cm^2)	W (S $s^{1/2}$ cm^{-2})
AZ31	2.23×10^{-4}	1.00	8.81×10^{2}	1.69×10^{-5}	0.83	3.93×10^{3}	—
50	8.26×10^{-7}	1.00	1.26×10^{6}	4.26×10^{-7}	0.19	5.77×10^{4}	1.83×10^{-7}
60	4.71×10^{-8}	0.56	4.44×10^{6}	3.09×10^{-11}	0.97	1.77×10^{5}	4.02×10^{-7}
70	6.60×10^{-7}	0.61	1.09×10^{6}	1.01×10^{-7}	0.39	2.79×10^{4}	1.42×10^{-6}
80	5.16×10^{-6}	0.78	6.03×10^{4}	3.49×10^{-6}	0.69	5.36×10^{3}	1.10×10^{-6}

corrosion resistance. The thickness, uniform and compact are the key factors affecting the corrosion resistance of the coating. The CaP coating prepared at 60 °C with uniform coverage on the surface of the AZ31B substrate exhibits the best corrosion resistance (Fig. 2–4).

Fig. 8 shows the EIS spectra for the uncoated substrate and the coated samples are evaluated in SBF solution at 37 °C. In the Nyquist spectra (Fig. 8(a) and (b)), the CaP coatings show much larger capacitive arcs compared with the uncoated AZ31B substrate, and larger radius of capacitive arc represents a better corrosion performance.[41] Thus the corrosion resistance of the AZ31B substrate is significantly improved after the preparation of the CaP coating. Among the four CaP coatings, the coating prepared at 60 °C has the highest capacitive arc resistance, reaching 5×10^6 Ω cm^2, indicating it has the best corrosion resistance. In the Bode–frequency plots (Fig. 8(c)), the impedance modulus at lower frequency is often used to evaluate the anticorrosion performance of coatings. The $|Z|_{0.1Hz}$ value of the CaP coating prepared at 60 °C is the largest among the four coatings, reaching 6.3×10^6 Ω cm^2, followed by the coating prepared at 50 °C with the $|Z|_{0.1Hz}$ value of 2.5×10^6 Ω cm^2, the coating prepared at 70 °C with the $|Z|_{0.1Hz}$ value of 7.9×10^5 Ω cm^2, and finally the coating prepared at 80 °C with the $|Z|_{0.1Hz}$ value of 5.5×10^4 Ω cm^2. Obviously, the $|Z|_{0.1Hz}$ value of the CaP coatings is much greater than the AZ31B substrate, which is only 5.0×10^3 Ω cm^2.

To further quantitatively analyze the protective behavior of different CaP coating, two equivalent circuit modes are established to fit the EIS date as shown in Fig. 8(e) and (f). The equivalent circuit mode of R(Q(R(QR))) (Fig. 8(e)) is used to describe the uncoated AZ31 substrate, where R_s is the solution resistance, CPE_{film} and R_{film} are the capacitance and resistance of magnesium oxide or hydroxide layer on AZ31 substrate, and CPE_{dl} and R_{ct} are the double electric layer capacitance and charge transfer resistance. The equivalent circuit mode of R(Q(R(Q(RW)))) (Fig. 8(f)) is used to depict the CaP coatings, where R_s is the solution resistance, CPE_{film} and R_{film} are the CaP coating on AZ31B substrate, and CPE_{dl} and R_{ct} are the double electric layer capacitance and charge transfer resistance.

And Warburg element (W) represented linear semi-infinite diffusion. The fitting parameters of AZ31B substrate and CaP coatings in SBF solution is shown in Table 2. The value of R_{film} and R_{ct} for CaP coatings much larger than that of AZ31B substrate, indicating the CaP coating can protect effectively the AZ31B magnesium substrate in SBF solution. Meanwhile, the CaP coating prepared at 60 °C exhibits the highest value of R_{film} and R_{ct} among the four coatings, indicating optimal corrosion resistance due to its dense structure and thicker thickness. To evaluate the stability of the CaP coating, long-term immersion test was carried out in SBF solution at 37 °C. Fig. 9(a) depicts the surface morphology of the CaP coating prepared at 60 °C after 21 days of immersion. It is clear that the surface morphology of the CaP coating undergo a significant change after 21 days immersion because most of the coating flakes off and exposes a large area of the substrate, and the Ca and P elements drastically reduced. Fig. 9(b) is the FTIR spectra of the CaP coating after immersion for 21 days. The reflection peaks at 1018 cm^{-1} are confirmed PO_4^{3-} group, and the peaks at about 540 cm^{-1} are due to P–O–P bending modes of HPO_4^{2-} ion.[36] Fig. 9(c)–(f) shows the XPS spectra of the CaP coating after immersion for 21 days. The atom percentage of Mg elements of the plated surface increases from 1.05 at% to 9.86 at% after immersion (Fig. 9(c)). Further analysis revealed that the content of DCPD in the coating decreases, while the content of $Mg(OH)_2$ and MgO

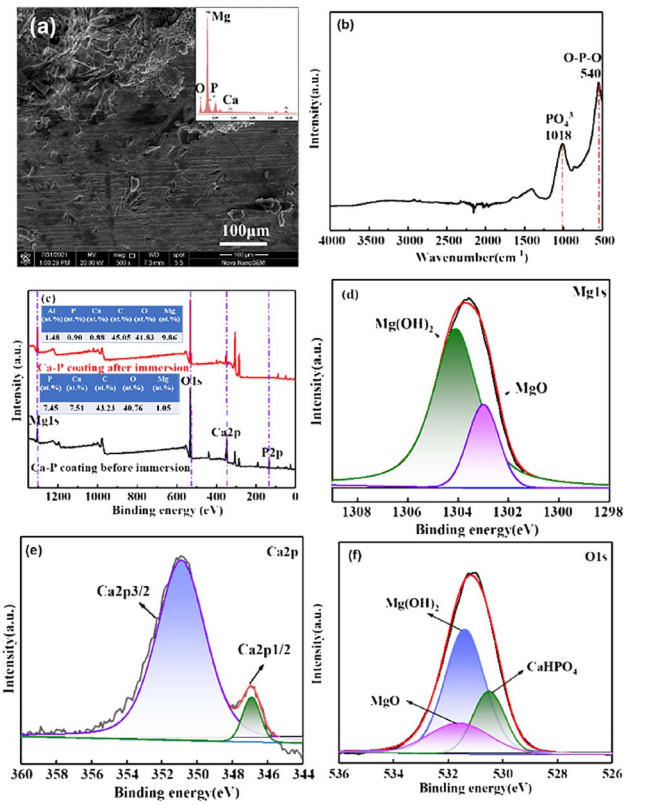

Fig. 9 (a) SEM, (b) FTIR spectra, (c) XPS survey spectra, and (d–f) the high-resolution XPS spectra of Mg, Ca and O of DCPD coating after immersion 21 days.

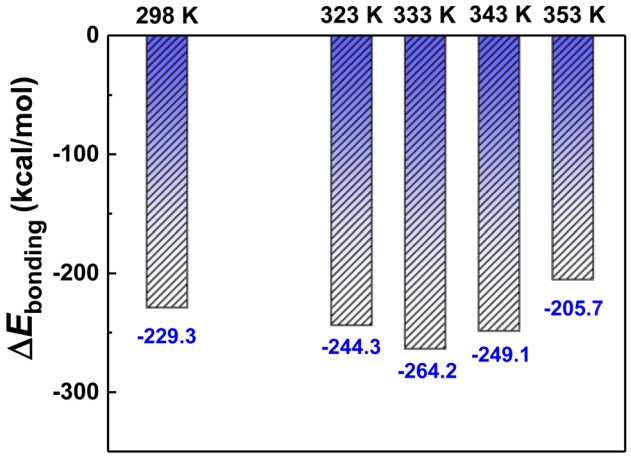

Fig. 10 $\Delta E_{bonding}$ of Mg/DCPD at different temperatures.

increases as shown in Fig. 9(d)–(f), indicating some parts of the coating have corroded leaving the substrates exposed. The result show that the bonding force between the CaP coating and the magnesium substrate is weak, and improving the bonding force of the coating will largely enhance its protection effectiveness of the coating.

4. Discussions

4.1 Interfacial binding energy of DCPD and Mg at different temperatures

MD simulations are used to investigate the interfacial bonding mechanism between DCPD coatings and Mg substrates. The Mg(0001) surface is chosen as the reaction surface, and the (−120) crystal surface of $CaHPO_4 \cdot 2H_2O$ is constructed above it. The bonding strength of $CaHPO_4 \cdot 2H_2O$ with Mg at different temperatures is characterized by the binding energy ($\Delta E_{bonding}$), which is calculated as follows:[42]

$$\Delta E_{bonding} = E_{Mg/DCPD} - E_{Mg} - E_{DCPD} \quad (1)$$

where $E_{Mg/DCPD}$ represents the total energy of the system when the Mg/DCPD system reaches steady state, E_{Mg} represents the total energy of Mg at steady state, E_{DCPD} represents the total energy of the DCPD coating at steady state. The $\Delta E_{bonding}$ of Mg/DCPD system at 298 K, 323 K, 333 K, 343 K and 353 K are −229.3 kcal mol^{-1}, −244.3 kcal mol^{-1}, −264.2 kcal mol^{-1}, −249.1 kcal mol^{-1} and −205.7 kcal mol^{-1}, respectively. According to the thermodynamic theory, when the value of $\Delta E_{bonding} < 0$, there is a certain bonding force between the two phases, and the

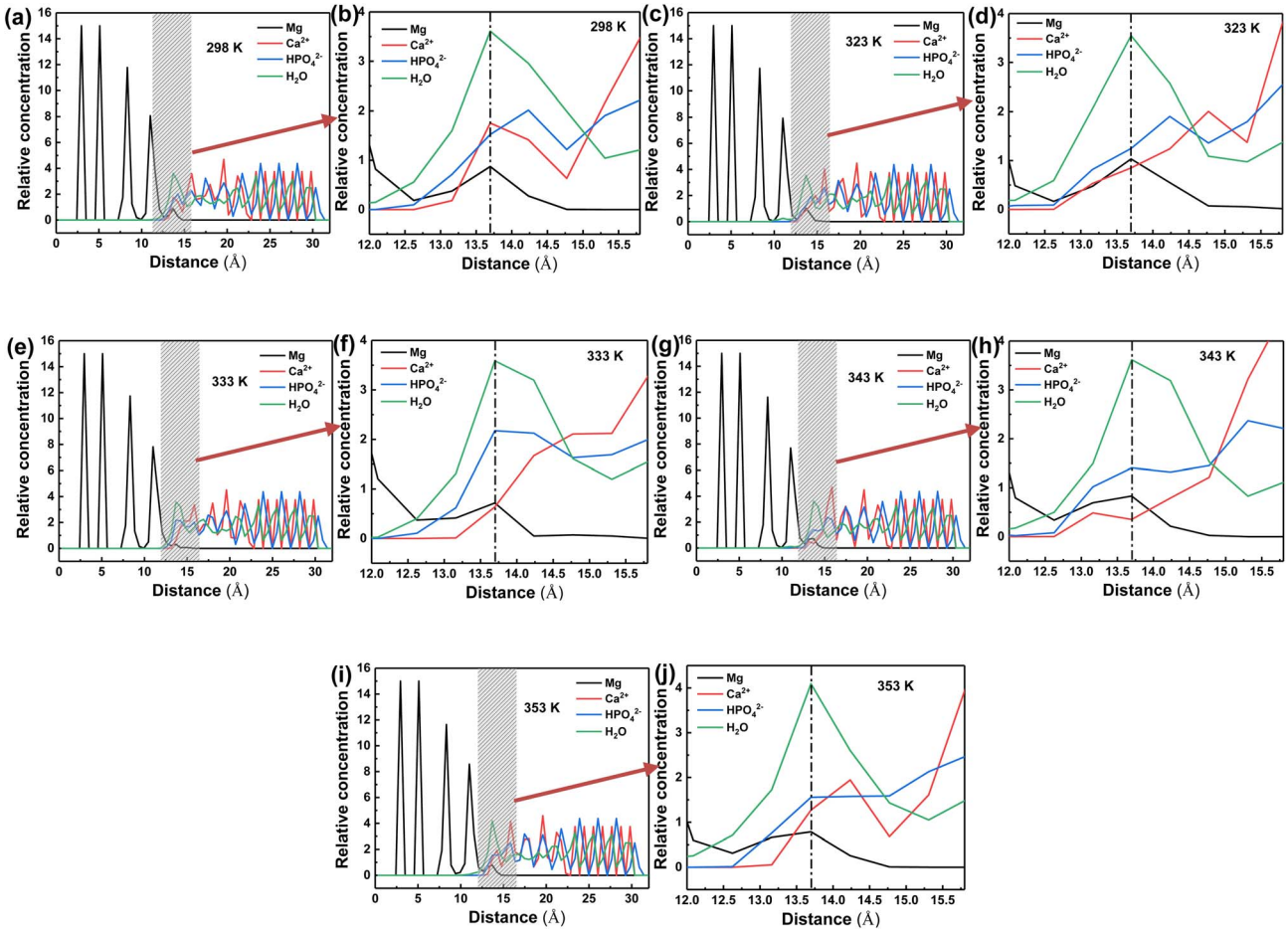

Fig. 11 Relative concentration of Mg, Ca^{2+}, HPO_4^{2-} and H_2O at different temperature: 298 K (a and b); 323 K (c and d); 333 K (e and f); 343 K (g and h); 353 K (i and j).

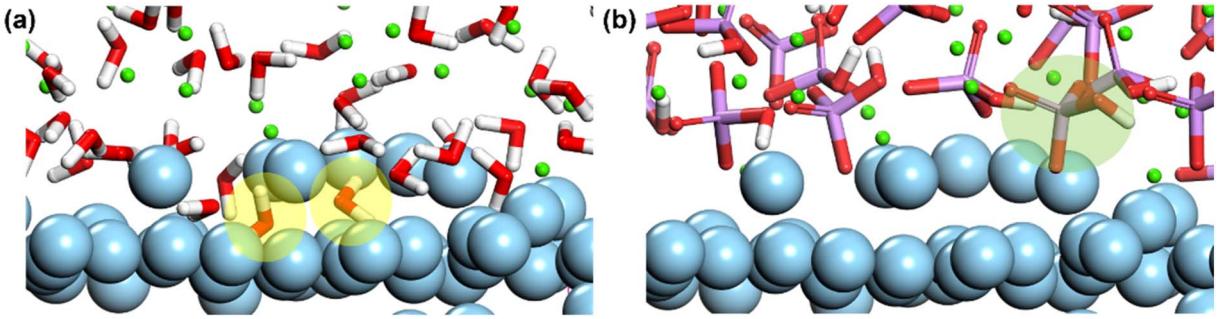

Fig. 12 Snapshots of the H_2O (a) and HPO_4^{2-} (b) on the interface of Mg.

larger the absolute value, the greater the bonding force.[43] Therefore, the interfacial binding between DCPD and Mg is a spontaneous process at 298 K–353 K, but the system has the lowest binding energy at 333 K, so the DCPD/Mg interface has the best bonding force at this temperature (Fig. 10).

In order to investigate the "rivet" groups that play a major role in the interfacial bonding of DCPD/Mg system, the concentration distribution of Ca^{2+}, HPO_4^{2-} and H_2O groups contained in the structure of $CaHPO_4 \cdot 2H_2O$ along the *Z*-axis (001) at different temperatures are analysed, as shown in Fig. 11. It is found that Mg and DCPD interpenetrated each other to form an obvious interfacial layer (shown in gray in Fig. 11(a), (c), (e), (g) and (i)). The distribution of HPO_4^{2-}, Ca^{2+}, Mg and H_2O in the interfacial layer in shown in Fig. 11(b), (d), (f), (h) and (j). The distribution of HPO_4^{2-} groups in the interfacial phase is the most, followed by H_2O, and the distribution of Ca^{2+} is the least. Therefore, HPO_4^{2-} and H_2O are the main groups that play the role of "rivet" in the interfacial bonding between DCPD and Mg. Compared with other temperatures, HPO_4^{2-} and H_2O are more distributed in the interfacial layer at 333 K, indicating that DCPD has stronger bonding force with Mg at 333 K.

Fig. 12 are the microstructures of Mg–HPO_4^{2-} and Mg–H_2O in the DCPD/Mg interfacial layer at 333 K. In order to form an effective bond with the Mg atoms, the O atoms close to Mg both show a certain conformational rotation. Among them, H_2O molecules are small enough to enter the Mg lattice and form lattice intercalation with Mg (Fig. 12(a) yellow circle), while HPO_4^{2-} is not able to enter the Mg lattice and forms mainly surface adsorption with Mg (Fig. 12(b) green circle). Therefore, compared with HPO_4^{2-}, H_2O is more likely to form stable bonding with Mg through structural changes.

5. Conclusion

The effect of plating temperature on the properties of the electroplating CaP coatings on magnesium alloy surface was studied carefully by experiments and computer simulations, and the following conclusions were obtained:

(1) The crystal morphology of CaP coatings gradually changed from dendritic lamellar structure to granular structure with the increasing of plating temperature, and the coating deposited at high temperature (80 °C) has poor bonding.

(2) The main structure of CaP coatings prepared at all four temperatures was DCPD, in addition to a small amount of HA.

(3) Potentiodynamic and EIS results show that the corrosion resistance of CaP coatings showed a trend of first increasing and then decreasing with the increase of plating temperature, and the coating prepared at 60 °C had the lowest corrosion current density and the best corrosion resistance.

(4) The computer simulation results showed that the interfacial binding energy between DCPD and Mg was negative, indicating that the interfacial binding between DCPD and Mg was a spontaneous process. The H_2O and HPO_4^{2-} in the structure of DCPD were widely distributed at the interface and play a "riveting" role in the DCPD/Mg interfacial phase. The binding energy of DCPD/Mg system is lowest at 60 °C, coupled with H_2O and HPO_4^{2-} were most distributed at the interface at this temperature, so the coating prepared at 60 °C has excellent binding force and corrosion resistance properties.

Author contributions

Jing Yuan: investigation, validation, writing-original draft, writing-review & editing, funding acquisition. Bin Dai: investigation, formal analysis. Xiaofeng Cui: formal analysis. Pei Li: supervision, project administration, funding acquisition.

Conflicts of interest

The authors declare that they have no known competing financial interests or personal relationships that could have appeared to influence the work reported in this paper.

Acknowledgements

This paper was supported by Thousand Talents Plan for High-end Innovative Talents in Qinghai Province, the Western Light Talents Training Program of Chinese Academy of Sciences and the Guiding Plan of Qinghai Provincial Health Commission (No. 2021-wjzdx-33).

References

1 L. Ling, S. Cai, Q. Li, J. Sun, X. Bao and G. Xu, Recent advances in hydrothermal modification of calcium

phosphorus coating on magnesium alloy, *J. Magnesium Alloys*, 2022, **10**, 62–80.
2 S. Agarwal, J. Curtin, B. Duffy and S. Jaiswal, Biodegradable magnesium alloys for orthopaedic applications: a review on corrosion, biocompatibility and surface modifications, *Mater. Sci. Eng., C*, 2016, **68**, 948–963.
3 X. L. Liu, T. Feng, G. M. Chen, S. F. Wen, J. H. Ding, H. J. Lin and Z. F. Yue, Effect of carbon interface on adhesion and anti-corrosion properties of hydroxyapatite coating on AZ31 magnesium alloy, *Mater. Chem. Phys.*, 2022, **287**, 126351.
4 T. X. Wang, Y. Q. Dong, Y. C. Xu, G. Y. Li, Y. T. Guo, J. S. Lian, Z. H. Zhang and L. Q. Ren, A calcium phosphate coating improving corrosion resistance of the biodegradable magnesium alloy with graphene oxide modifying the deposition, *Ceram. Int.*, 2023, **49**, 11926–11935.
5 K. Mohemi, T. Ahmadi, A. Jafarzadeh, H. R. Bakhsheshi-Rad, M. Taghian Dehaghani and F. Berto, Synthesis, corrosion, and bioactivity evaluation of the hybrid anodized polycaprolactone fumarate/silicon and magnesium co-doped fluorapatite nanocomposite coating on AZ31 magnesium alloy, *Phys. Mesomech.*, 2022, **25**, 85–96.
6 Z. Zhang, J. X. Xie, J. H. Zhang, H. Dong, S. J. Liu, X. B. Zhang, J. Wang and R. Z. Wu, Simultaneously improving mechanical and anti-corrosion properties of extruded Mg-Al dilute alloy via trace Er addition, *J. Mater. Sci. Technol.*, 2023, **150**, 49–64.
7 L. Telmenbayar, A. G. Ramu, D. Yang and D. J. Choi, Development of mechanically robust and anticorrosion slippery PEO coating with metal–organic framework (MOF) of magnesium alloy, *Chem. Eng. J.*, 2023, **458**, 141397.
8 N. M. Huang, Y. Wang, Y. Zhang, L. Liu, N. Y. Yuan and J. N. Ding, Multifunctional coating on magnesium alloy: superhydrophobic, self-healing, anti-corrosion and wear-resistant, *Surf. Coat. Technol.*, 2023, **463**, 129539.
9 M. N. Sarian, N. Iqbal, P. Sotoudehbagha, M. Razavi, Q. U. Ahmed, C. Sukotjo and H. Hermawan, Potential bioactive coating system for high-performance absorbable magnesium bone implants, *Bioact. Mater.*, 2022, **12**, 42–63.
10 Y. C. Ma, M. Talha, Q. Wang, N. T. Zhou, Z. H. Li and Y. H. Lin, A multifunctional coating with modified calcium phosphate/chitosan for biodegradable magnesium alloys of implants, *New J. Chem.*, 2022, **46**, 4436–4448.
11 M. Rahman, Y. C. Li and C. E. Wen, Realization and characterization of double-layer Ca-P coating on WE43 Mg alloy for biomedical applications, *Surf. Coat. Technol.*, 2020, **398**, 126091.
12 Y. C. Su, C. J. Lu, X. L. Hu, Y. T. Guo, X. C. Xun, Z. H. Zhang, G. Y. Li, J. S. Lian and L. Q. Ren, Improving the degradation resistance and surface biomineralization ability of calcium phosphate coatings on a biodegradable magnesium alloy via a sol-gel spin coating method, *J. Electrochem. Soc.*, 2018, **165**, C155–C161.
13 Y. T. Guo, Y. C. Su, R. Gu, Z. H. Zhang, G. Y. Li, J. S. Lian and L. Q. Ren, Enhanced corrosion resistance and biocompatibility of biodegradable magnesium alloy modified by calcium phosphate/collagen coating, *Surf. Coat. Technol.*, 2020, **401**, 126318.
14 T. J. Liu, Y. Li, Y. Zhang, M. Zhao, Z. H. Wen and L. M. Zhang, A biodegradable, mechanically tunable micro-arc oxidation AZ91D-based composite implant with calcium phosphate/chitosan coating promotes long-term bone tissue regeneration, *Biotechnol. J.*, 2021, **16**, 2000653.
15 A. Ali, F. Iqbal, A. Ahmad, F. Ikram, A. Nawaz, A. A. Chaudhry, S. A. Siddiqi and I. Rehman, Hydrothermal deposition of high strength calcium phosphate coatings on magnesium alloy for biomedical applications, *Surf. Coat. Technol.*, 2019, **357**, 716–727.
16 W. Zai, S. Sun, H. C. Man, J. S. Lian and Y. S. Zhang, Preparation and anticorrosion properties of electrodeposited calcium phosphate (CaP) coatings on Mg–Zn–Ca metallic glass, *Mater. Chem. Phys.*, 2022, **290**, 126532.
17 M. Horynová, M. Remešová, L. Klakurková, K. Dvořák, I. Ročňáková, S. K. Yan, L. Čelko and G. L. Song, Design of tailored biodegradable implants: the effect of voltage on electrodeposited calcium phosphate coatings on pure magnesium, *J. Am. Ceram. Soc.*, 2018, **102**, 123–135.
18 M. Uddina, C. Hall and V. Santos, Fabrication, characterisation and corrosion of HA coated AZ31B Mg implant material: effect of electrodeposition current density, *Surf. Coat. Technol.*, 2020, **385**, 125363.
19 F. Pastorek, B. Hadzima, M. Omasta and M. Mhaede, Effect of electrodeposition temperature on corrosion resistance calcium phosphate, *Acta Metall. Slovaca*, 2014, **20**, 200–208.
20 W. Lu, C. W. Ou, Z. L. Zhan, P. Huang, B. Yan and M. S. Chen, Microstructure and in vitro corrosion properties of ZK60 magnesium alloy coated with calcium phosphate by electrodeposition at different temperatures, *Int. J. Electrochem. Sci.*, 2013, **8**, 10746–10757.
21 S. Yazdani, L. Prince and V. Vitry, Optimization of electroless Ni single bond B-nanodiamond coating corrosion resistance and understanding the nanodiamonds role on pitting corrosion behavior using shot noise theory and molecular dynamic simulation, *Diamond Relat. Mater.*, 2023, **134**, 109793.
22 R. Hsissou, F. Benhiba, S. Abbout, O. Dagdag, S. Benkhaya, A. Berisha, H. Erramli and A. Elharfi, Trifunctional epoxy polymer as corrosion inhibition material for carbon steel in 1.0 M HCl: MD simulations, DFT and complexation computations, *Inorg. Chem. Commun.*, 2020, **115**, 107858.
23 G. Bahlakeh, B. Ramezanzadeh and M. Ramezanzadeh, The role of chrome and zinc free-based neodymium oxide nanofilm on adhesion and corrosion protection properties of polyester/melamine coating on mild steel: experimental and molecular dynamics simulation study, *J. Cleaner Prod.*, 2019, **210**, 872–886.
24 H. Y. Wang, H. N. Yuan, J. M. Wang, E. G. Zhang, M. Y. Bai, Y. F. Sun, J. F. Wang, S. J. Zhu, Y. F. Zheng and S. K. Guan, Influence of the second phase on protein adsorption on biodegradable Mg alloys' surfaces: comparative experimental and molecular dynamics simulation studies, *Acta Biomater.*, 2021, **129**, 323–332.
25 W. Shang, F. Wu, S. Q. Jiang, Y. Q. Wen, N. Peng and J. Q. Jiang, Effect of hydrophobicity on the corrosion resistance of microarc oxidation/self-assembly/nickel

composite coatings on magnesium alloys, *J. Mol. Liq.*, 2021, **330**, 115606.

26 K. F. Wang, M. H. Wang, Q. G. Wang, X. Lu and X. D. Zhang, Computer simulation of proteins adsorption on hydroxyapatite surfaces with calcium phosphate ions, *J. Eur. Ceram. Soc.*, 2017, **37**, 2509–2520.

27 Q. S. Dong, X. X. Zhou, Y. J. Feng, K. Qian, H. Liu, M. M. Lu, C. L. Chu, F. Xue and J. Bai, Insights into self-healing behavior and mechanism of dicalcium phosphate dihydrate coating on biomedical Mg, *Bioact. Mater.*, 2021, **6**, 158–168.

28 F. Abbona, F. Christensson, M. F. Angela and H. E. L. Madsen, Crystal habit and growth conditions of brushite, $CaHPO_4 \cdot 2H_2O$, *J. Cryst. Growth*, 1993, **131**(3–4), 331–346.

29 H. Y. Wang, Z. Fang, Y. Zhao, S. C. Yao, J. F. Wang, S. J. Zhu, C. Y. Niu, Y. Jia and S. K. Guan, Effects of alloy elements on adsorption of fibrinogen on biodegradable magnesium alloys surfaces: the MD simulations and experimental studies, *Appl. Surf. Sci.*, 2020, **512**, 145725.

30 H. S. Su, Y. Liu, X. Gao, Y. F. Qian, W. J. Li, T. G. Ren, L. Wang and J. L. Zhang, Corrosion inhibition of magnesium alloy in NaCl solution by ionic liquid: synthesis, electrochemical and theoretical studies, *J. Alloys Compd.*, 2019, **791**, 681–689.

31 N. A. Curry and D. W. Jones, Crystal structure of brushite, calcium hydrogen orthophosphate dihydrate: a neutron-diffraction investigation, *J. Chem. Soc. A*, 1971, 3725–3729.

32 C. A. Beevers, The crystal structure of dicalcium phosphate dihydrate, $CaHPO_4 \cdot 2H_2O$, *Acta Crystallogr.*, 1958, **11**(4), 273–277.

33 L. F. Sukhodub, L. B. Sukhodub, W. Simka and M. Kumeda, Hydroxyapatite and brushite coatings on plasma electrolytic oxidized Ti_6Al_4V alloys obtained by the thermal substrate deposition method, *Mater. Lett.*, 2019, **250**, 163–166.

34 N. Aboudzadeh, C. Dehghanian and M. A. Shokrgozar, Effect of electrodeposition parameters and substrate on morphology of Si-HA coating, *Surf. Coat. Technol.*, 2019, **375**, 341–351.

35 A. Rafeek, G. Choi and L. Evans, Morphological, spectroscopic and crystallographic studies of calcium phosphate bioceramic powders, *J. Australas. Ceram. Soc.*, 2018, **54**, 161–168.

36 S. Turk, I. Altinsoy, G. CelebiEfe, M. Ipek, M. Ozacar and C. Bindal, Biomimetric coating of monophasic brushite on Ti6Al4V in new m-5xSBF, *Surf. Coat. Technol.*, 2018, **351**, 1–10.

37 S. Koburger, A. Bannerman, L. Grover, F. Muller, J. Bowen and J. Paxton, A novel method for monitoring mineralisation in hydrogels at the engineered hard-soft tissue interface, *Biomater. Sci.*, 2014, **2**, 41–51.

38 R. Barua, C. Daly-Seiler, Y. Chenreghanianzabi, D. Markel, Y. W. Li, M. Zhou and W. P. Ren, Comparing the physicochemical properties of dicalcium phosphate dihydrate (DCPD) and polymeric DCPD (P-DCPD) cement particles, *J. Biomed. Mater. Res.*, 2021, **109**, 1644–1655.

39 X. Li, X. Liu, S. Wu, K. Yeung, Y. Zheng and P. K. Chu, Design of magnesium alloys with controllable degradation for biomedical implants: from bulk to surface, *Acta Biomater.*, 2016, **45**, 2–30.

40 J. G. Acheson, L. Robinson, S. McKillop, S. Wilson, M. J. McIvor, B. J. Meenan and A. R. Boyd, TOFSIMS and XPS characterisation of strontium in amorphous calcium phosphate sputter deposited coatings, *Mater. Charact.*, 2021, **171**, 110739.

41 J. Yuan, R. Yuan, J. H. Wang, Q. S. Li, X. T. Xing, X. Liu and W. B. Hu, Fabrication and corrosion resistance of phosphate/ZnO multilayer protective coating on magnesium alloy, *Surf. Coat. Technol.*, 2018, **352**, 74–83.

42 G. G. Zhou, G. W. Lu, Y. Q. Jiao, Y. F. Li, K. Wang and Y. X. Yu, A molecular simulation study on adsorption behavior of solid-liquid interface in KDP crystal, *Acta Phys. Sin.*, 2012, **61**, 010204.

43 J. Z. Liu, B. Yu and Q. Z. Hong, Molecular dynamics simulation of distribution and adhesion of asphalt components on steel slag, *Constr. Build. Mater.*, 2020, **255**, 119322.